Composite Structures 189 (2018) 586–597

Contents lists available at ScienceDirect

Composite Structures

journal homepage: www.elsevier.com/locate/compstruct

Hoberman-sphere-inspired lattice metamaterials with tunable negative thermal expansion

Yangbo Li[a,b], Yanyu Chen[c], Tiantian Li[b], Siyu Cao[a], Lifeng Wang[b,*]

[a] *College of Hydraulic and Environmental Engineering, China Three Gorges University, Yichang, Hubei 443002, China*
[b] *Department of Mechanical Engineering, State University of New York at Stony Brook, Stony Brook, NY 11794, USA*
[c] *Transportation and Hydrogen Systems Center, National Renewable Energy Laboratory, Golden, CO 80401, USA*

ARTICLE INFO

Keywords:
Metamaterials
Lattice
Negative thermal expansion

ABSTRACT

Materials with engineered thermal expansion coefficients, capable of avoiding failure or irreversible destruction of structures and devices, are important for aerospace, civil, biomedical, optics, and semiconductor applications. In natural materials, thermal expansion usually cannot be adjusted easily and a negative thermal expansion coefficient is still uncommon. Here we propose a novel architected lattice bi-material system, inspired by the Hoberman sphere, showing a wide range of tunable thermal expansion coefficient from negative to positive, $-1.04 \times 10^{-3}\,°\mathrm{C}^{-1}$ to $1.0 \times 10^{-5}\,°\mathrm{C}^{-1}$. Numerical simulations and analytical formulations are implemented to quantify the evolution of the thermal expansion coefficients and reveal the underlying mechanisms responsible for this unusual behavior. We show that the thermal expansion coefficient of the proposed metamaterials depends on the thermal expansion coefficient ratio and the axial stiffness ratio of the constituent materials, as well as the bending stiffness and the topological arrangement of the constitutive elements. The finding reported here provides a new routine to design architected metamaterial systems with tunable negative thermal expansion for a wide range of potential applications.

1. Introduction

Architected lattice metamaterials with multiple length scales enable the design of new material systems with unprecedented properties, such as negative thermal expansion (NTE) [1,2], negative Poisson's ratio [3–7], ultralightweight and ultrahigh stiffness [8,9], negative stiffness [10], improved thermal resistance [11], and tunable phononic [12] and photonic [13] properties. Especially, their emergence has reactivated researches on NTE materials. Most of natural solid materials have positive thermal expansion, suggesting that they will expand when heated and shrink when cooled due to the elongation or shortening of interatomic bonds. Researchers have found several exceptional natural examples such as zeolites [14], and synthesized composites with NTE, such as $PbTiO_3$/Cu composites [15] and cement/ZrW_2O_8 composites [16], which are usually synthesized by integrating each other in nano- or micro-particles before sintering or solidification. However, they only manifest NTE in a narrow range. Furthermore, these synthesized composites have random microstructures, indicating that the NTE cannot be tailored readily. In order to extensively mitigate the thermal twist, buckle and distortion [17], thermomechanical failure [18], and fatigue [19] from thermal stress mismatch and maintain the geometric stability [1,2], engineers and material scientists have turned their interests on exploring novel metamaterials with negative thermal expansion. Compared with conventional synthesized composites with random microstructures, lattice metamaterials fabricated by three-dimensional (3D) printing technique and with well-defined topologies can give rise to tunable NTE. The exceptional thermal properties, zero or extremely low thermal expansion, make these metamaterials ideal candidates that can maintain precise dimensional tolerances for many potential engineering applications under large temperature fluctuations in service environments, including aerospace structures, civil engineering structures, optical instruments, biomedical engineering, and semiconductors.

With the rapid progress of additive manufacturing technique, many recent breakthroughs have been achieved in the design of metamaterials from different aspects, such as material compositions, fabrication methods, and modeling approaches. Novel structures of unit cells used in lattice metamaterials have been proposed and can be summarized as: (1) bi-material triangles or the derivatives [2,20–36], (2) chirality [37–41], (3) bilayer buckling origami or trusses [37,42–45], and (4) re-entrant structures [3,28]. As far as compositions of materials are concerned, metal [21,25–31,36–40,46–48], soft polymer [35,38,43,45], composites [2,43] or combination of the aforementioned three [24]

---

[*] Corresponding author.
E-mail address: lifeng.wang@stonybrook.edu (L. Wang).

https://doi.org/10.1016/j.compstruct.2018.01.108
Received 17 October 2017; Received in revised form 26 January 2018; Accepted 31 January 2018

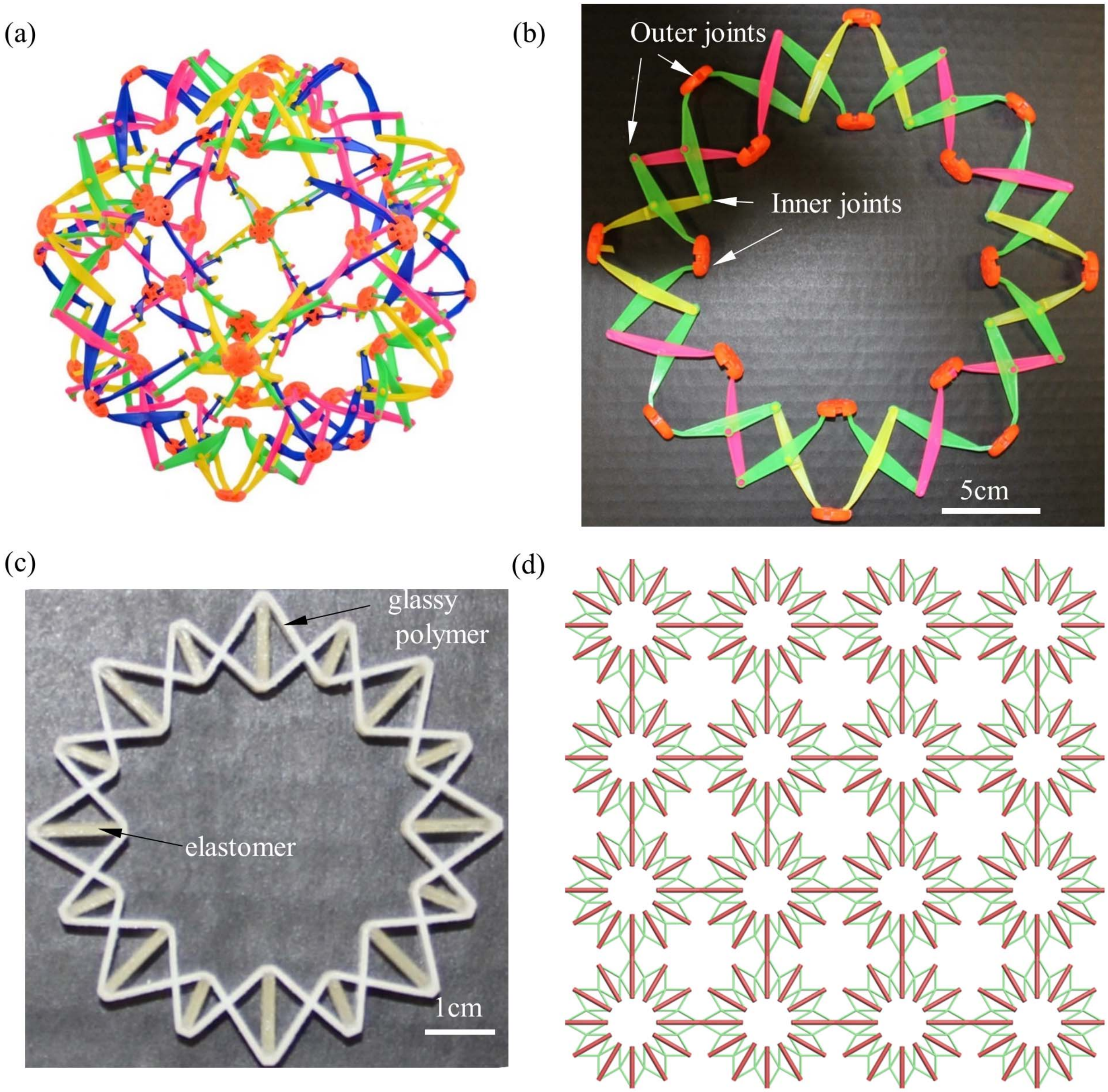

Fig. 1. Design of the lattice metamaterials with tunable thermal expansion: (a) Hoberman expandable sphere, (b) the planar element, (c) the unit cell fabricated by 3D printing technique, and (d) the lattice metamaterial with 4 × 4 unit cells.

have been adopted. In terms of fabrication methods, these metamaterials have been fabricated by welding [21,25,37], micro-stereolithography [2,22], 3D printing [38], laser cut [27], metal lift-off process [46], liquid photoresist and laser lithography [45], and sintering [36]. The thermal expansion coefficient of these metamaterials have also been evaluated through theoretical [23,29,30,32–34,39,40,44,47,49], and numerical [20–22,24,28,31,37,45,48] analyses. Among these artificially designed NTE metamaterials, lattice metamaterials with bi-materials and void space are possible to be adjusted through the volume or area change when the temperature changes. Those researches have enriched tremendously the members of the warehouse of lattice metamaterials with zero or negative thermal expansion. There are other novel existing structures to be referred to pursue NTE like the Hoberman sphere [50]. Moreover, theoretical analysis models and fabrications of those metamaterials with tunable NTE are still evolving, which makes it possible to design more novel NTE structures.

Here, inspired by the Hoberman sphere shown in Fig. 1, we present a class of bi-material lattice metamaterials that can be explored to achieve tunable thermal expansion. The mechanism of the NTE effect depends on its scissors-like microstructure and the circular arrangement of the bi-material triangles. We theoretically and numerically investigate the thermomechanical response of the proposed metamaterials by varying geometric parameters and mechanical properties. A quantitative model considering constituents' axial and bending stiffness is developed to understand the contribution of the NTE mechanism during the thermal variation process. The model also provide the dependence of the NTE on the constituents' mechanical properties and topological features. Finite element simulations are performed to analyze the source of the NTE and are compared with the theoretical model predictions. These models quantify how this negative CTE can be engineered by tailoring the shape, the size, the number of bi-material triangle units, and beams' cross-sectional geometry, providing a viable avenue to analyze the effective CTE of other NTE structures.

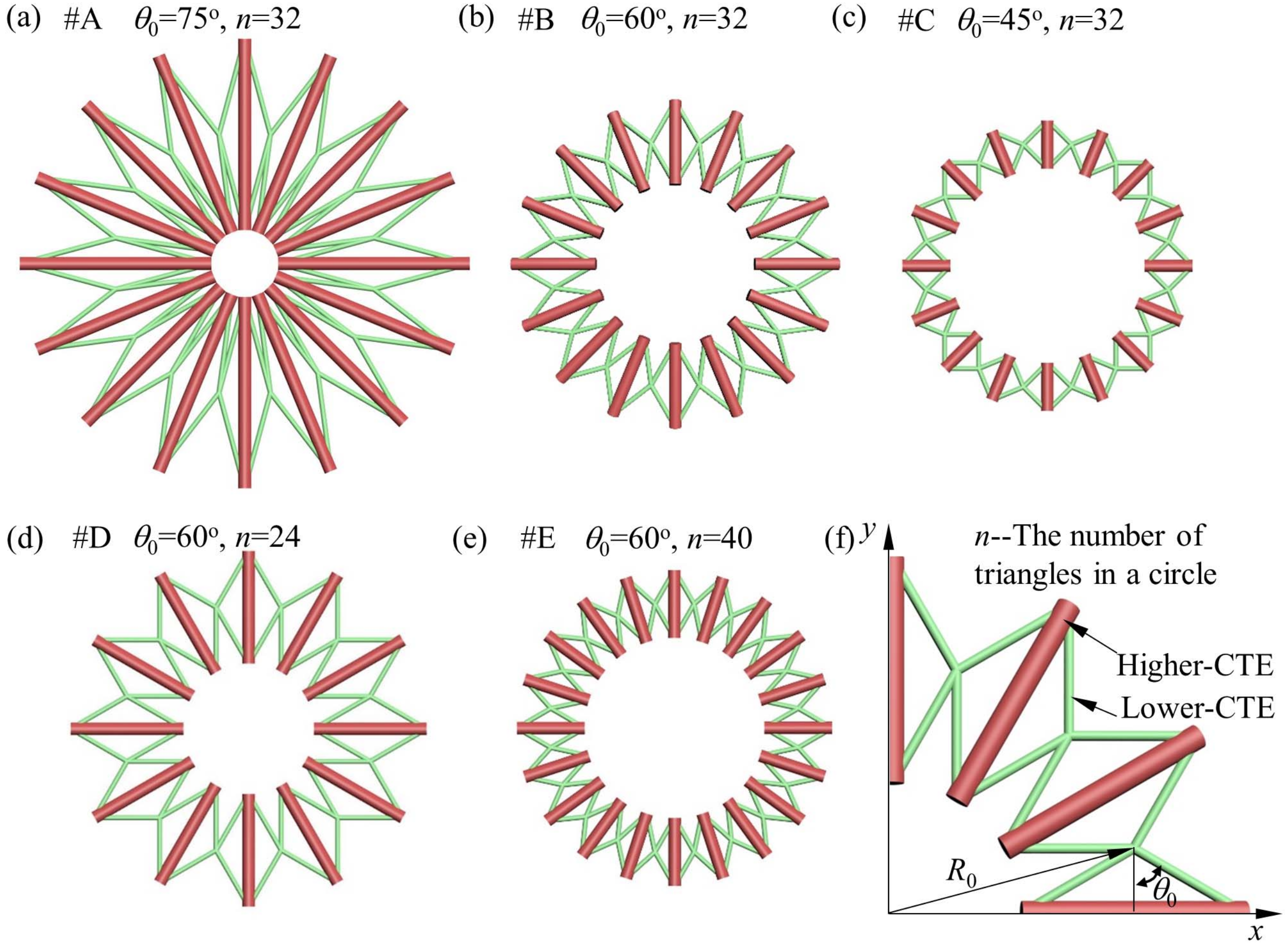

Fig. 2. Representative unit cells of the proposed lattice metamaterials. Those unit cells including (a)–(e) are characterized by the radius of the circle (distance between the center and green cross point) R_0 with R_0 = 10 mm, the half vertex angle between blue beams in the triangle θ_0, and the number of triangles in a circle, n. (f) One quarter unit cell with definitions including R_0, θ_0, and n, as well as Higher-CTE (the material of higher coefficient of thermal expansion), Lower-CTE (the material of lower coefficient of thermal expansion) constituents. (For interpretation of the references to color in this figure legend, the reader is referred to the web version of this article.)

2. Models and methods

2.1. Characterization of lattice metamaterials

The design concept is inspired by the Hoberman's expandable sphere (see Fig. 1(a)), which is an isokinetic structure that resembles a geodesic dome. It is capable of folding down to a fraction of its normal size by the scissor-like action of the joints. When it contracts, the distance of outer and inner joints elongates. Referring to its geometric features and deformation mechanisms, we propose a class of unit cells with NTE, which inherit scissor-like geodesic circle (see Fig. 1(b)). We append a linking beam in the outer and inner joints and change hinges into fixed joints, as shown in Fig. 1(c) where the designed unit cell is fabricated using 3D printing technique. The unit cells are characterized by the radius of circular arrangement, R_0, the number of triangles, n, and half vertex angle of the triangle, θ_0, as shown in Fig. 2. As R_0, n, and θ_0 vary, we can construct a series of unit cells, #A to #E.

The unit cell of the proposed lattice metamaterials is made up of n totally identical bi-material isosceles triangles (see Figs. 2 and 3), one of which is composed of a base member (red beam) with a higher coefficient of thermal expansion (higher-CTE), α_h, and two legs (blue beams) with a lower coefficient of thermal expansion (lower-CTE), α_l (Fig. 3). Those triangles are evenly distributed in a polar pattern around a center point, and some of them share a base, while others have a common vertex. Blue and red beams expand at different rates when heated: the blue beams are induced to fold toward the red beams, compressing the voids and ultimately occupying less space, vice versa, as shown in Fig. 3(a)–(b). Because of the circular pattern, the circumferential compression squeezes further the central voids, which magnifies the strain rate of the unit cell, vice versa.

2.2. Analytical model

Since the idealized circle is centrally symmetrical, it can be divided into n segments of equal arcs, one of which is approximately equal to the height of the triangle, h_0. It is the fundamental module characterized by minimum contracted or expanded element illustrated in Fig. 3(c). When the temperature changes from T_0 to $T_0+\Delta T$, the shrinkage or elongation of the circular arrangement, or triangles ring chain from nh_0 to nh leads to its own circumference longer or shorter. To retain the entire circular shape, radius reduction or expansion appears from R_0 to R, which indicates the negative thermal expansion in the proposed metamaterials. To avoid local buckling in compressive beams, we limit θ_0 in the interval [30°, 75°]. We assume that (1) all the constituents are elastic, recoverable, and small deformable materials, and (2) during the thermal deformation, the angle φ keeps approximately constant as shown in Fig. 3(c).

In the representative isosceles triangle in Fig. 3(c), its height, the length of its base or higher-CTE beam, and the length of its leg or lower-CTE beam are $h_0 = R_0\sin\varphi$, $l_0 = 2R_0\sin\varphi\tan\theta_0$, and $m_0 = \frac{R_0\sin\varphi}{\cos\theta_0}$, respectively. The initial distance between the center and the outer endpoint S_0 is expressed as

$$s_0 = R_0(\cos\varphi + \sin\varphi\tan\theta_0), \tag{1}$$

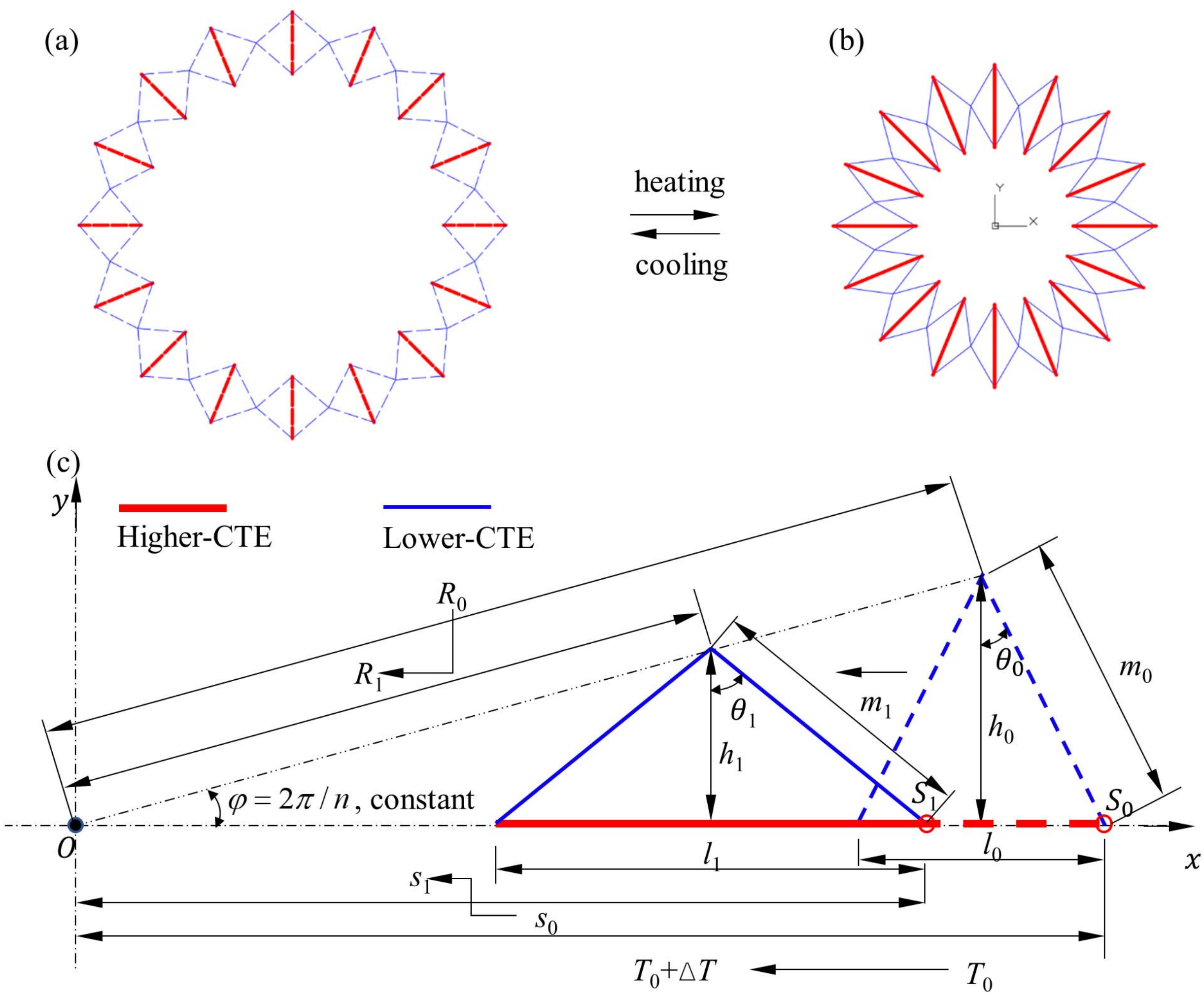

Fig. 3. Theoretical model of thermal deformation of the unit cell. (a) The unit cell before heated, (b) the unit cell after heated, and (c) the representative element of the unit cell, or bi-material isosceles triangle, where T_0 and $T_0 + \Delta T$ denote the initial temperature, and the temperature after heated, respectively. R_0 is the initial radius of the circle, θ_0 the initial angle between the height and the leg of the triangle, m_0 the initial length of the leg of the triangle, l_0 initial length of base line of the triangle, s_0 the initial distance between the origin O and the outer endpoint S_0, h_0 the initial height of the triangle. When the temperature changes, R_0, θ_0, m_0, l_0, s_0, and h_0 change into R, θ, m, l, s, and h, respectively.

where the central angle $\varphi = 2\pi/n$, keeps approximately constant. The distance between the center and the outer endpoint S changes into

$$s = s_0 + u_1, \tag{2}$$

where u_1 is the horizontal displacement of the outer point S. And the strain of the entire unit cell is described isotopically as

$$\varepsilon = \frac{s-s_0}{s_0}. \tag{3}$$

Substituting Eqs. (1)–(3) to $\alpha = \frac{\varepsilon}{\Delta T}$, we can obtain effective CTE as

$$\alpha = \frac{1}{\Delta T}\frac{u_1}{R_0(\cos\varphi + \sin\varphi\tan\theta_0)}, \tag{4}$$

where u_1 is the key factor which solves α. Due to highly central symmetry, the solution of u_1 relies on the representative isosceles triangle, which consists of three clamped beams with symmetric boundary conditions along the axes OX and OG as shown in Fig. 4(c). It can be solved by the displacement method in structural mechanics using beam element in Fig. 4(a). Nodal forces and moments are denoted as $\{U_i \quad V_i \quad M_i\}^{\mathrm{T}}$, and $\{U_j \quad V_j \quad M_j\}^{\mathrm{T}}$, and nodal displacements and rotations as $\{u_i \quad v_i \quad \varphi_i\}^{\mathrm{T}}$, and $\{u_j \quad v_j \quad \varphi_j\}^{\mathrm{T}}$ at Node i and j in a beam element on the local coordinate system. The element local stiffness matrix is conducted as

$$[k]^e = \begin{bmatrix} \frac{AE}{l} & 0 & 0 & -\frac{AE}{l} & 0 & 0 \\ 0 & \frac{12EI}{l^3} & \frac{6EI}{l^2} & 0 & \frac{-12EI}{l^3} & \frac{6EI}{l^2} \\ 0 & \frac{6EI}{l^2} & \frac{4EI}{l} & 0 & \frac{-6EI}{l^2} & \frac{2EI}{l} \\ -\frac{AE}{l} & 0 & 0 & \frac{AE}{l} & 0 & 0 \\ 0 & \frac{-12EI}{l^3} & \frac{-6EI}{l^2} & 0 & \frac{12EI}{l^3} & \frac{-6EI}{l^2} \\ 0 & \frac{6EI}{l^2} & \frac{2EI}{l} & 0 & \frac{-6EI}{l^2} & \frac{4EI}{l} \end{bmatrix}, \tag{5}$$

where A is the sectional area, E is the Young's Modulus, I is the inertia moment, and l is the length of the beam element in the local coordinate system in Fig. 4(a).

The element nodal forces and displacements meet

$$\{F\} = [k]^e\{\delta\}, \tag{6}$$

where the element nodal force is $\{F\} = \{U_iV_iM_iU_jV_jM_j\}^{\mathrm{T}}$, and the element nodal displacement is $\{\delta\} = \{u_iv_i\varphi_iu_jv_j\varphi_j\}$ as shown in Fig. 4(a). When the global coordinate system is transformed from the local coordinate system as shown in Fig. 4(b), the element global stiffness matrix is expressed as

$$[K]^e = [h]^T[k]^e[h], \tag{7}$$

where $[h]$ is the coordinate transformation matrix as

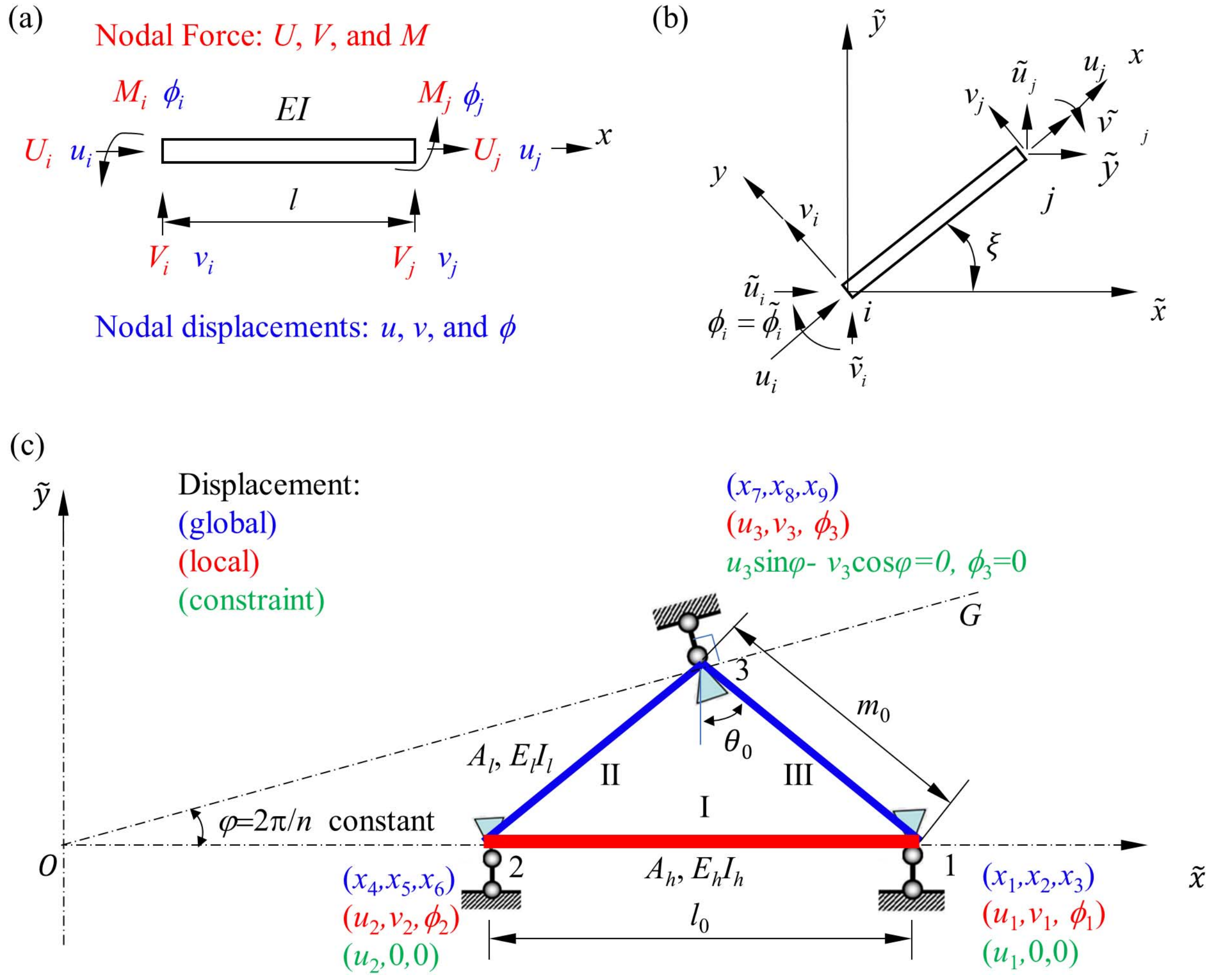

Fig. 4. Beam element and representative isosceles triangle frame with boundary conditions. (a) Beam element with nodal displacements, rotations, forces, and moments. (b) Conversion from the local system to the global system. (c) Elements, nodes, and constraint conditions. The global elements are I, II and III. The global nodes are designated as 1, 2 and 3. The global nodal displacements are x_1, x_2, x_3, x_4, x_5, x_6, x_7, x_8 and x_9. A_l, E_l and I_l are the sectional area, Young's Modulus and the inertia moment of the lower-CTE beam, respectively. A_h, E_h and I_h are the sectional area, Young's Modulus and the inertia moment of the higher-CTE beam, respectively.

$$[h] = \begin{bmatrix} \cos\xi & \sin\xi & 0 & 0 & 0 & 0 \\ -\sin\xi & \cos\xi & 0 & 0 & 0 & 0 \\ 0 & 0 & 1 & 0 & 0 & 0 \\ 0 & 0 & 0 & \cos\xi & \sin\xi & 0 \\ 0 & 0 & 0 & -\sin\xi & \cos\xi & 0 \\ 0 & 0 & 0 & 0 & 0 & 1 \end{bmatrix}, \tag{8}$$

and ξ is the angle between local and global x-axis along the clockwise direction. The three elements' stiffness matrices are listed as Appendix A. The global stiffness matrix $[K]$ is assembled as Appendix (A4).

As shown in Fig. 4(c), the triangular frame's boundary conditions are described as

$$\begin{cases} x_2 = 0; x_3 = 0; \\ x_5 = 0; x_6 = 0; \\ x_7\sin\varphi - x_8\cos\varphi = 0; x_9 = 0; \end{cases}, \tag{9}$$

where $\{X\} = \{x_1\ x_2\ x_3\ x_4\ x_5\ x_6\ x_7\ x_8\ x_9\}^{\mathrm{T}}$ defines global nodal displacements. Element local thermal load, $\{P_T^e\} = \{EA\alpha\Delta T\ \ 0\ \ 0\ \ -EA\alpha\Delta T\ \ 0\ \ 0\}^{\mathrm{T}}$, is transformed to the global coordinate system by $\{P_T\} = [h]^{\mathrm{T}}\{P_T^e\}$. Assembling global stiffness matrix and calculating thermal loads, we produce a 9 × 9 symmetric linear equations as $[K]\{u\} = \{P\}$. Dealing with the boundary conditions, we obtain a solution with respect to$\{u_1 u_2 u_3\}^{\mathrm{T}}$,which is the solution of $[K']\{u\} = \{P'\}$ or

$$\begin{bmatrix} K'_{11} & K'_{12} & K'_{13} \\ K'_{21} & K'_{22} & K'_{23} \\ K'_{31} & K'_{32} & K'_{33} \end{bmatrix} \begin{Bmatrix} u_1 \\ u_2 \\ u_3 \end{Bmatrix} = \begin{Bmatrix} P'_1 \\ P'_2 \\ P'_3 \end{Bmatrix}. \tag{10}$$

More details are listed in Appendix A.

After solving the linear equations, and substituting them to Eq. (4), we can calculate the effective CTE. So, Eqs. (4) and (9) are used to describe the effective CTE of proposed metamaterials. The *LU* Decomposition Method is adopted to solve Eq. (9) using FORTRAN. The effective CTE, α, is associated with E_h, A_h, α_h, E_l, A_l, I_l, α_l, θ_0 and φ. Furthermore, it is relevant to the CTE ratio of the Higher-CTE beam and the lower-CTE beam, $\frac{\alpha_h}{\alpha_l}$, and the axial stiffness ratio, $\frac{A_hE_h}{A_lE_l}$ of Higher-CTE and Lower-CTE beams, as well as bending stiffness, $\frac{I_l}{A_l}$ of the lower-CTE beam, and irrelevant to increment temperature, ΔT, within the linear elastic range.

2.3. Finite element simulations

To verify the theoretical models and better understand the behavior of the proposed metamaterials, we investigate their thermal responses through numerical simulations with the finite element Abaqus/Standard package. In all simulations, we consider a quarter of a unit cell with suitable periodic boundary conditions. 2D solid models are constructed using 4-node bilinear plane stress element CPS4R. No out-of-plane deformation is allowed in the current study. Thermal load is considered for the temperature change from 20 °C to 70 °C.

Table 1
Mechanical properties of adopted bi-material combinations.

Higher/Lower-CTE	PEGDA/Cu-PEGDA	Teflon/Acrylic	Al/Ti	Al/Invar	A/B
E_h, E_l (GPa) α_h, α_l(10^{-6} °C^{-1})	0.0235, 0.1124 155.6, 39.8	0.475, 3.2 123, 67	70, 116 23.1, 8.6	70, 144 23.1, 1.1	10, 10 200, 20
E_h/E_l	0.21	0.15	0.603	0.486	1
α_h/α_l	3.91	1.84	2.686	21	10

Parametric studies in geometry and mechanical properties have been conducted using the unit cell-based finite element models and theoretical models. We build models of the unit cells with $R_0 = 10$ mm, $24 \le n \le 40$, and $30° \le \theta_0 \le 75°$, and compare numerical and theoretical results based on possible constituents mentioned in the literature [2,27,28,51]. Table 1 lists several material combinations and customized materials (A/B) with $E_h = 10$ GPa, $\alpha_h = 2 \times 10^{-4}$ °C^{-1}, $E_l = 10$ GPa, $\alpha_l = 2 \times 10^{-5}$ °C^{-1}, and $\nu_h = \nu_l = 0.3$. We also vary the ratio of two constituents' CTE α_h/α_l from 10.0 to 1.0, the ratio of two constituents' sectional area, A_h/A_l from 10.0 to 0.1, and the ratio of two constituents' Young's Modulus E_h/E_l from 0.001 to 1000 in our parametric studies.

3. Results and discussion

3.1. Existence of negative thermal expansion

Fig. 5 shows a good agreement between theoretical and numerical results, although the elastic 2D solid element deforms essentially more than the beam element. Fig. 5(a)–(c) displays that NTE phenomenon clearly occur in the unit cells #A, #B, and #D. As the temperature increases, all higher-CTE beams moving inward actuate the shrinkage

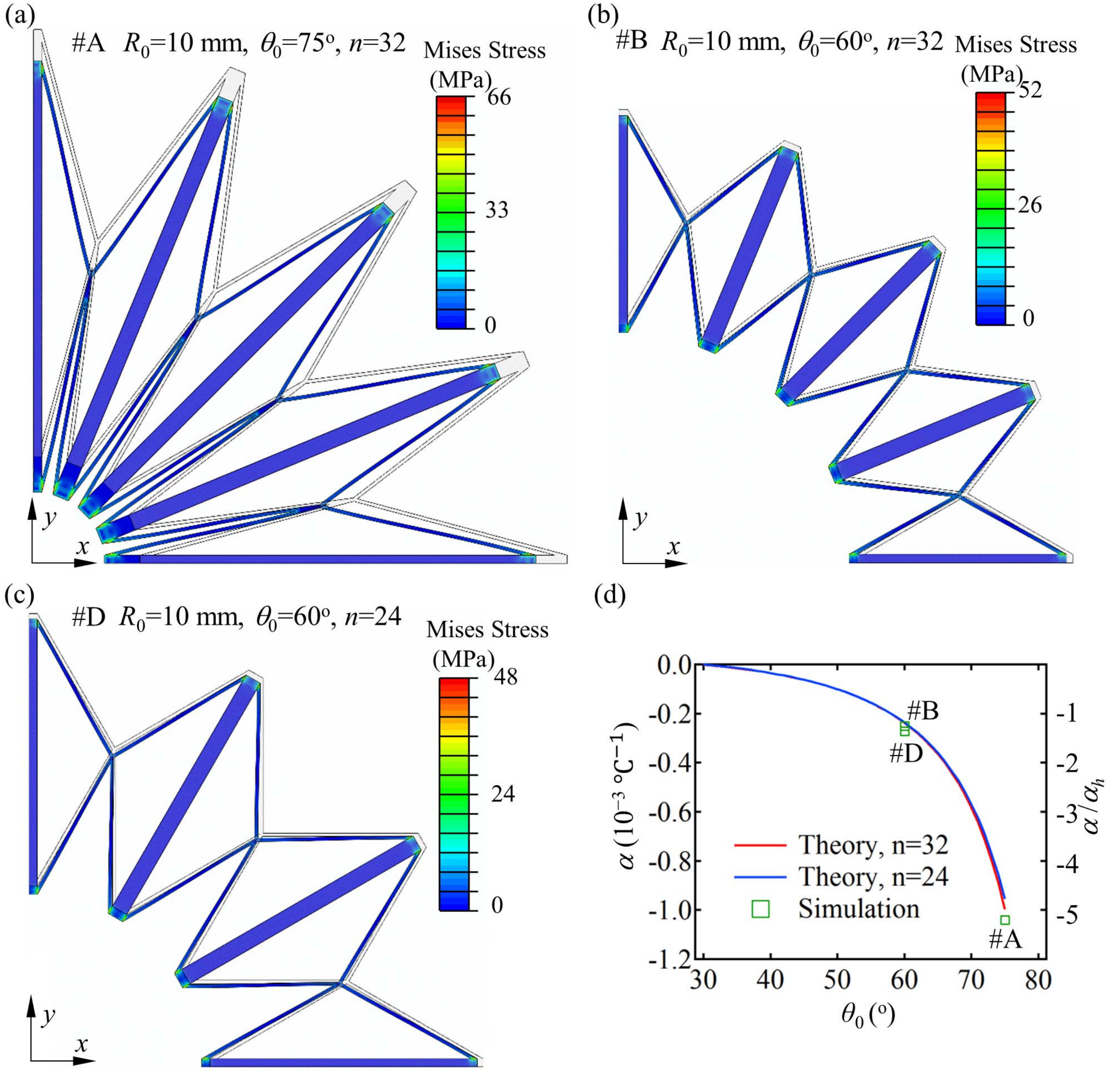

Fig. 5. Mises stress contours as well as numerical and theoretical comparison of a quarter of cooled metamaterial unit cells including #A in (a), #B in (b), #D in (c), as $\Delta T = 50$ °C, $A_h/A_l = 5$, $\alpha_h/\alpha_l = 10$, $E_h/E_l = 1$ and $\alpha_h = 2 \times 10^{-4}$ °C^{-1}. (d) The effective CTE and normalized effective CTE of the unit cells with $30° \leqslant \theta_0 \leqslant 75°$ as well as $n = 24$ and $n = 32$ using theoretical models and numerical simulations. The color scale bars of Mises stress are linear.

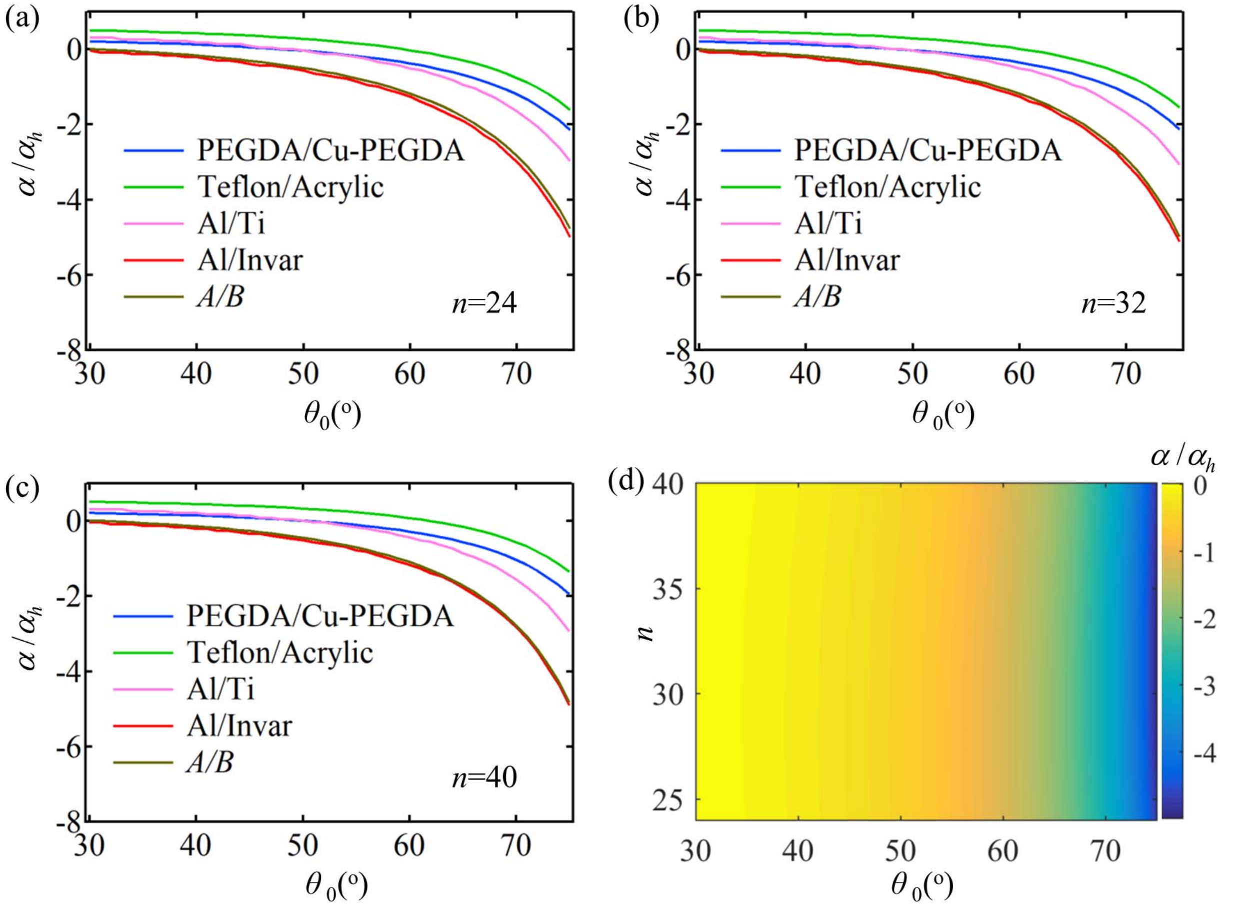

Fig. 6. The normalized effective CTE of the lattice metamaterials with $\theta_0 \in [30^\circ, 75^\circ]$, $n \in [24^\circ, 40^\circ]$, $\Delta T = 50\,^\circ\mathrm{C}$, using different bi-material combinations. (a) Normalized effective CTE versus θ_0 with $n = 24$, $30^\circ \leqslant \theta_0 \leqslant 75^\circ$. (b) Normalized effective CTE versus θ_0 with $n = 32$, $30^\circ \leqslant \theta_0 \leqslant 75^\circ$. (c) Normalized effective CTE versus θ_0 with $n = 40$, $30^\circ \leqslant \theta_0 \leqslant 75^\circ$. (d) Normalized effective CTE using customized materials (A/B) with $E_h = 10\,\mathrm{GPa}$, $\alpha_h = 2 \times 10^{-4}\,^\circ\mathrm{C}^{-1}$, as well as $E_l = 10\,\mathrm{GPa}$, $\alpha_l = 2 \times 10^{-5}\,^\circ\mathrm{C}^{-1}$.

of the entire unit cell. As shown in Fig. 5(d), both numerical analysis and theoretical models show that the value of NTE rises with the increase of the angle θ_0. As expected, the thermal expansion is almost independent of n. The maximum NTE happens with normalized effective $\alpha/\alpha_h = -5.2$ and $\alpha = -1.04 \times 10^{-3}\,^\circ\mathrm{C}^{-1}$ when θ_0 of the unit cell is 75°.

The theoretical and numerical investigations verify that tunable or negative thermal expansion does occur among those proposed metamaterials in a wide range. The elongation or contraction of the higher-CTE beams induces triangles flattened or sharpened, which causes the triangle circumference shorter or longer after heated or cooled. The NTE effect of this scissors-like and ring-like configuration is clearly demonstrated in this study.

3.2. Effect of geometric parameters

The NTE in the proposed metamaterials provides us flexible space on selecting suitable constituents. We chose alternative metallic and polymeric materials mentioned above to investigate the correlation between NTE and geometric parameters.

Fig. 6 shows the normalized effective CTE of the lattice metamaterials considering different bi-material combinations. Note that when θ_0 is small, the metamaterials with three material combinations (Teflon/Acrylic, Al/Ti, and PEGDA/Cu-PEGDA) have positive CTEs. When θ_0 is greater than 50°, the CTE becomes negative. However, the metamaterials with A/B and Al/Invar combinations exhibit negative CTEs with θ_0 from 30° to 75°, and decreases as θ_0 increases. Fig. 6(d) provides the contour of the normalized effective CTE of the lattice metamaterials with $30^\circ \le \theta_0 \le 75^\circ$, $24 \le n \le 40$ using customized materials (A/B), indicating the impact of θ_0 and n on the normalized effective CTE. Clearly, the angle θ_0 plays a more significant role in the negative CTE, indicating tuning of CTE with well-designed angle θ_0. The number n has less effect on the CTEs, which is confirmed in Fig. 7. In general, the effective CTE is more sensitive to θ_0 than n, while it is irrelevant to R_0. It's also observed that when θ_0 is smaller than 60°, the normalized CTE of all metamaterials is between -2 and 0.2. However, when θ_0 is larger such as 75° as shown in Fig. 7(c), the normalized CTE can be small from -5.2 to $-1.04 \times 10^{-3}\,^\circ\mathrm{C}^{-1}$. The metamaterial with Teflon/Acrylic combination always has larger CTEs, but the metamaterial with Al/Invar combination has the smallest CTEs due to the higher ratio of CTEs.

3.3. Effect of mechanical properties

Considering that the normalized effective CTE of #A is the smallest (largest in absolute value) among all unit cells listed in Fig. 2, we take metamaterial #A as a representative example to analyze the effect of the mechanical properties on the CTE. Fig. 8 depicts the evolution of the effective CTE of metamaterial #A as a function of CTE ratio α_h/α_l and the ratio of Young's modulus, E_h/E_l, where $\Delta T = 50\,^\circ\mathrm{C}$. Clearly the normalized effective CTE strongly depends on both CTE ratio and Young's modulus ratio. When Young's modulus ratio is from $E_h/E_l = 0.001$ to $E_h/E_l = 0.01$, the normalized effective CTE is close to 0 for all α_h/α_l from 1 to 10. When E_h/E_l is larger than 0.01, the normalized effective CTE is positive when α_h/α_l is smaller than ~ 1.5; however, the normalized effective CTE turns negative when α_h/α_l is larger than ~ 1.5. Higher α_h/α_l indicates lower effective CTE. A minimum normalized effective CTE α/α_h emerges at -5.2 and $\alpha = -1.04 \times 10^{-3}\,^\circ\mathrm{C}^{-1}$ as

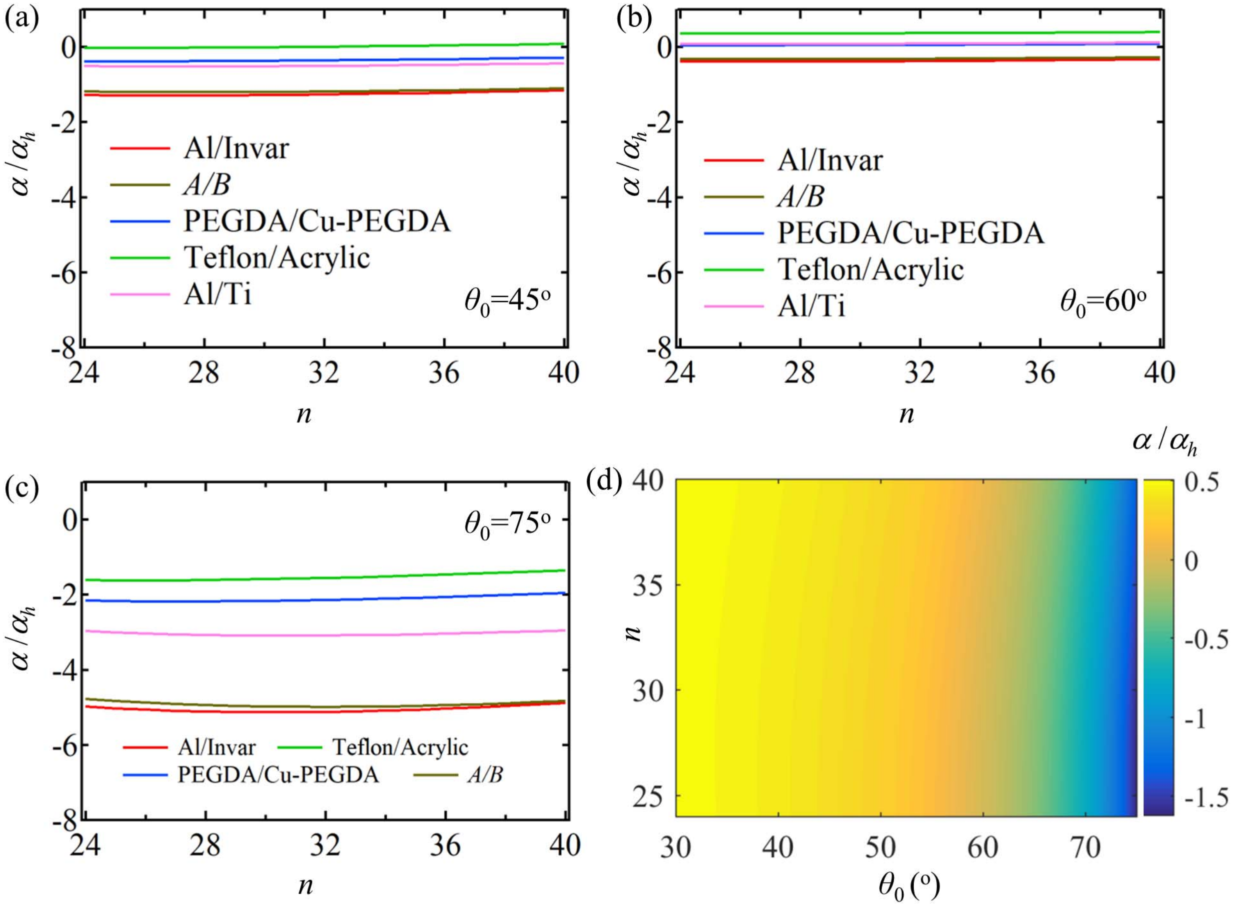

Fig. 7. The normalized effective CTE of the lattice metamaterials with $\theta_0 \in [30^\circ, 75^\circ]$, $n \in [24^\circ, 40^\circ]$, $\Delta T = 50\,^\circ\mathrm{C}$, using different bi-material combination. (a) Normalized effective CTE versus n with $\theta_0 = 45^\circ$, $24 \leqslant n \leqslant 40$. (b) Normalized effective CTE versus n with $\theta_0 = 60^\circ$, $24 \leqslant n \leqslant 40$. (c) Normalized effective CTE versus n with $\theta = 75^\circ$, $24 \leqslant n \leqslant 40$. (d) Normalized effective CTE as $30^\circ \leqslant \theta_0 \leqslant 75^\circ$, $24 \leqslant n \leqslant 40$ using Teflon/Acrylic.

shown in Fig. 8(b). In Fig. 8(c)–(d), for metamaterial #A with customized materials, we present the evolution of the normalized effective CTE as the function of the CTE ratio α_h/α_l and the sectional area ratio A_h/A_l, while $E_h/E_l = 1$ and $\Delta T = 50\,^\circ\mathrm{C}$. Similarly, for the sectional area ratio from 0.1 to 10, the normalized effective CTE is positive when α_h/α_l is smaller than ~ 1.5; however, the normalized effective CTE turns negative when α_h/α_l is larger than ~ 1.5. Dramatic changes are found for α_h/α_l increasing from 1 to 4.

To verify the results experimentally, a heating process (from 22.5 °C to 68.0 °C) is performed on the unit cell (see Fig. 1(c)) fabricated by a multiple material 3D printer (Objet260 Connex, Stratasys Ltd), where $A_h/A_l = 2$, $\alpha_h/\alpha_l = 1.5$ and $E_h/E_l = 0.0034$. The measured CTE of this sample is $2.9 \times 10^{-4}\,^\circ\mathrm{C}^{-1}$, which is consistent with the effective CTE as $2.2 \times 10^{-4}\,^\circ\mathrm{C}^{-1}$ predicted by our model, indicating a validation of our analytical model and simulation method. Note that this sample shows positive CTE, which is limited by the materials from our 3D printing method. However, by tuning the geometrical parameters and constituent materials' properties, the desired effective CTE of the bi-material lattice metamaterials can be achieved. In general, the primary influencing factor is the CTE ratio of higher-CTE and lower-CTE constituents; the secondary one is the sectional area ratio; and the third one is the ratio of Young's modulus. This finding suggests that the CTE can be tailored to be positive, zero, and even negative by controlling these effects, thereby offering opportunities to design lattice metamaterials with tunable CTE.

Furthermore, the stiffness of the NTE structures is crucial for potential applications. To study the mechanical properties especially the stiffness of the proposed metamaterials, uniaxial tension is carried out using finite element analysis. The details of the simulation can be found in Appendix B. The calculated Young's Modulus is shown in Table 2. Compared with their constituent materials, the proposed metamaterials exhibit relatively low stiffness because of their bending-dominated deformations of the lattice structures. However, they still have considerable load-carrying capability in addition to the unusual NTE property. Further work is needed to investigate the mechanical response of the proposed lattice metamaterials and seek the trade-off between the NTE and the stiffness in applications.

4. Conclusion

In summary, we have demonstrated an approach to create bi-material lattice metamaterials with tunable negative or extremely low thermal expansion coefficient from $-1.04 \times 10^{-3}\,^\circ\mathrm{C}^{-1}$ to $1.0 \times 10^{-5}\,^\circ\mathrm{C}^{-1}$, inspired by the Hoberman sphere. Through a combination of analytical analysis and numerical simulations, we have showed that the thermal expansion coefficient of the bi-material lattice metamaterials can be tuned by selecting the constituent materials with different thermal expansion coefficients, stiffness (tension/compression and bending), and the geometric parameters of the lattice metamaterials. In particular, the quantitative modeling of thermo-mechanical behavior presented here can precisely predict the thermal expansion coefficient of the bi-material lattice metamaterials. It can be envisioned that the proposed design strategy can be extended to 1D and 3D metamaterials, providing insights into the development of a new class of architected metamaterials with potential applications including aerospace industry, civil engineering, biomedical sensors, optics, and semiconductors.

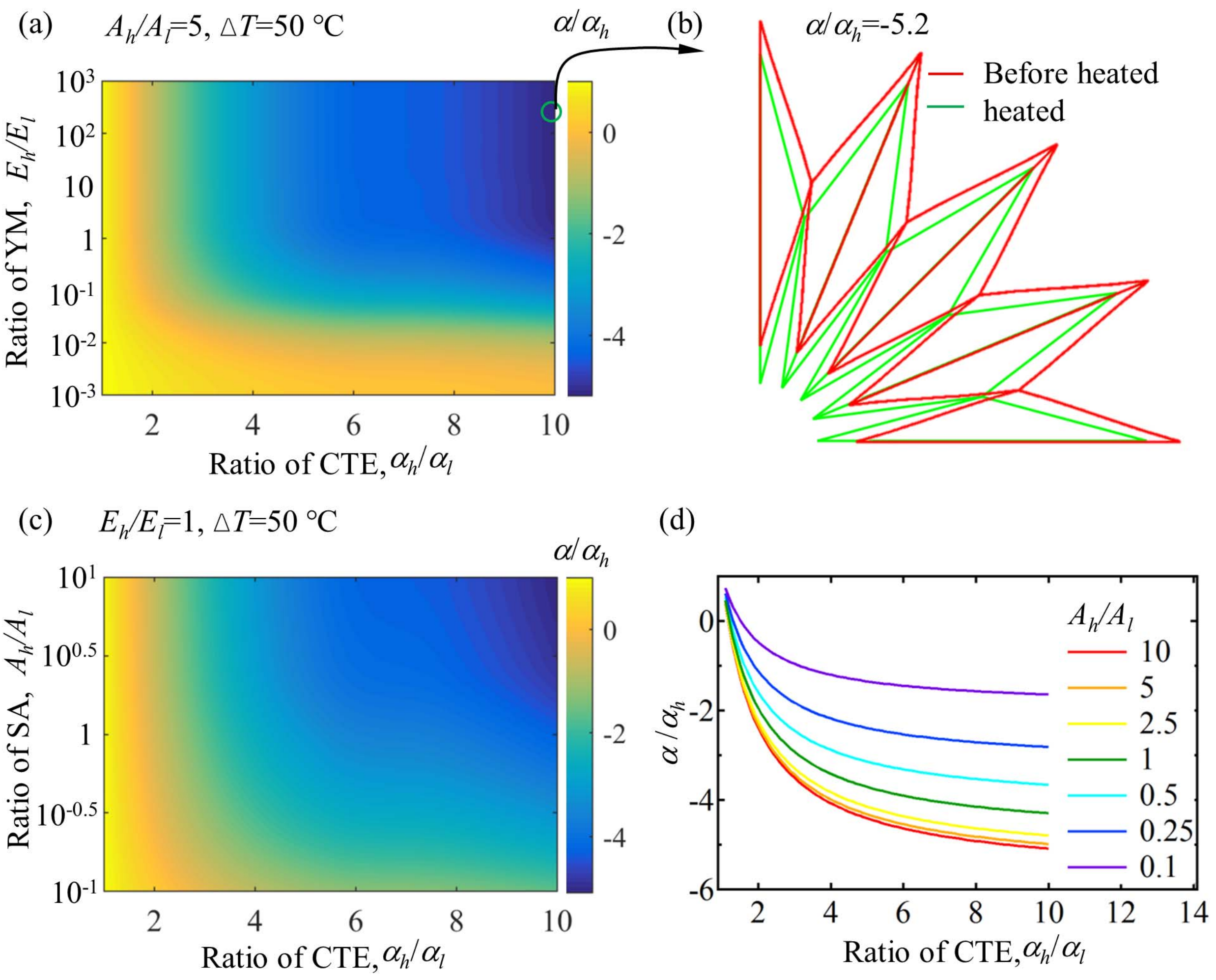

Fig. 8. The effect of mechanical properties on the CTE of metamaterial #A (R = 10 mm, θ_0 = 75°, n = 32). (a) Effective CTE of #A between α/α_h versus the ratio of CTE α_h/α_l, the ratio of Young's Modulus, E_h/E_l, and (b) the corresponding thermally deformed shape in theoretical model. (c) Normalized effective CTE of #A between α/α_h versus the ratio of CTE α_h/α_l, ratio of stiffness A_h/A_l. (d) Normalized effective CTE α/α_h, and the ratio of CTE α_h/α_l, of #A with the ratio of sectional area A_h/A_l=10, 5, 2.5, 1, 0.5, 0.25 and 0.1.

Table 2
The equivalent Young's modulus of the bi-material metamaterials ($\overline{V}$ is the volume fraction of the unit cell, $\overline{E}$ is the equivalent Young's modulus of the metamaterials, and E_0 is the Young's Modulus of the Lower-CTE material, MPa).

bi-material		PEGDA/Cu-PEGDA		Teflon/Acrylic		Al/Ti		Al/Invar		A/B	
Unit cell	$\overline{V}$	$\overline{E}$	$E_0\overline{V}$	$\overline{E}$	$E_0\overline{V}$	$\overline{E}$	$E_0\overline{V}$	$\overline{E}$	$E_0\overline{V}$	$\overline{E}$	$E_0\overline{V}$
#A	0.2045	3.5×10^{-3}	22	0.084	654.3	3.61	23.7×10^3	3.76	29.43×10^3	0.32	2044
#B	0.1349	4.6×10^{-3}	15.4	0.13	438.2	4.76	16×10^3	5.9	19.7×10^3	0.41	1350
#D	0.1248	4.8×10^{-3}	14	0.14	399.4	5.0	14×10^3	6.2	18×10^3	0.43	1248

Acknowledgements

The authors gratefully acknowledge the National Science Foundation (CMMI-1462270), the Region 2 University Transportation Research Center (UTRC), and the Office of Naval Research. The authors thank Xianlei Meng and Shuyuan Zhang (China Three Gorges University) for helping to prepare images. Y. Li gratefully acknowledges the financial support from the China Scholarship Council (File No. 201508420188).

Appendix A

The stiffness matrix of Element I is:

$$[K]_I^e = \begin{bmatrix} \frac{A_hE_h}{l_0} & 0 & 0 & -\frac{A_hE_h}{l_0} & 0 & 0 \\ 0 & \frac{12E_hI_h}{l_0^3} & \frac{-6E_hI_h}{m_0^2} & 0 & \frac{-12E_hI_h}{l_0^3} & \frac{-6E_hI_h}{l_0^2} \\ 0 & \frac{-6E_hI_h}{l_0^2} & \frac{4E_hI_h}{l_0} & 0 & \frac{6E_hI_h}{l_0^2} & \frac{2E_hI_h}{l_0} \\ -\frac{A_hE_h}{l_0} & 0 & 0 & \frac{A_hE_h}{l_0} & 0 & 0 \\ 0 & \frac{-12E_hI_h}{l_0^3} & \frac{6E_hI_h}{m_0^2} & 0 & \frac{12E_hI_h}{l_0^3} & \frac{6E_hI_h}{l_0^2} \\ 0 & \frac{-6E_hI_h}{l_0^2} & \frac{2E_hI_h}{l_0} & 0 & \frac{6E_hI_h}{l_0^2} & \frac{4E_hI_h}{l_0} \end{bmatrix}. \tag{A1}$$

The stiffness matrix of Element II is:

$$[k]_{II}^e = \begin{bmatrix} \frac{A_lE_l}{m_0}\sin^2\theta_0 + \frac{12E_lI_l}{m_0^3}\cos^2\theta_0 & (\frac{A_lE_l}{m_0} - \frac{12E_lI_l}{m_0^3})\sin\theta_0\cos\theta_0 & -\frac{6E_lI_l}{m_0^2}\cos\theta_0 & -\frac{A_lE_l}{m_0}\sin^2\theta_0 - \frac{12E_lI_l}{m_0^3}\cos^2\theta_0 & -(\frac{A_lE_l}{m_0} - \frac{12E_lI_l}{m_0^3})\sin\theta_0\cos\theta_0 & -\frac{6E_lI_l}{m_0^2}\cos\theta_0 \\ (\frac{A_lE_l}{m_0} - \frac{12E_lI_l}{m_0^3})\sin\theta_0\cos\theta_0 & \frac{A_lE_l}{m_0}\cos^2\theta_0 + \frac{12E_lI_l}{m_0^3}\sin^2\theta_0 & \frac{6E_lI_l}{m_0^2}\sin\theta_0 & -(\frac{A_lE_l}{m_0} - \frac{12E_lI_l}{m_0^3})\sin\theta_0\cos\theta_0 & -\frac{A_lE_l}{m_0}\cos^2\theta_0 - \frac{12E_lI_l}{m_0^3}\sin^2\theta_0 & \frac{6E_lI_l}{m_0^2}\sin\theta_0 \\ -\frac{6E_lI_l}{m_0^2}\cos\theta_0 & \frac{6E_lI_l}{m_0^2}\sin\theta_0 & \frac{4E_lI_l}{m_0} & \frac{6E_lI_l}{m_0^2}\cos\theta & \frac{-6E_lI_l}{m_0^2}\sin\theta & \frac{2E_lI_l}{m_0} \\ -\frac{A_lE_l}{m_0}\sin^2\theta_0 - \frac{12E_lI_l}{m_0^3}\cos^2\theta_0 & (\frac{12E_lI_l}{m_0^3} - \frac{A_lE_l}{m_0})\sin\theta_0\cos\theta_0 & \frac{6E_lI_l}{m_0^2}\cos\theta_0 & \frac{A_lE_l}{m_0}\sin^2\theta_0 + \frac{12E_lI_l}{m_0^3}\cos^2\theta_0 & (\frac{A_lE_l}{m_0} - \frac{12E_lI_l}{m_0^3})\sin\theta_0\cos\theta_0 & \frac{6E_lI_l}{m_0^2}\cos\theta_0 \\ (\frac{12E_lI_l}{m_0^3} - \frac{A_lE_l}{m_0})\sin\theta_0\cos\theta_0 & -\frac{A_lE_l}{m_0}\cos^2\theta_0 - \frac{12E_lI_l}{m_0^3}\sin^2\theta_0 & \frac{-6E_lI_l}{m_0^2}\sin\theta_0 & (\frac{A_lE_l}{m_0} - \frac{12E_lI_l}{m_0^3})\sin\theta_0\cos\theta_0 & \frac{A_lE_l}{m_0}\cos^2\theta_0 + \frac{12E_lI_l}{m_0^3}\sin^2\theta_0 & \frac{-6E_lI_l}{m_0^2}\sin\theta_0 \\ -\frac{6E_lI_l}{m_0^2}\cos\theta_0 & \frac{6E_lI_l}{m_0^2}\sin\theta_0 & \frac{2E_lI_l}{m_0} & \frac{6E_lI_l}{m_0^2}\cos\theta_0 & \frac{-6E_lI_l}{m_0^2}\sin\theta_0 & \frac{4E_lI_l}{m_0} \end{bmatrix}. \tag{A2}$$

The stiffness matrix of Element III is:

$$[k]_{III}^e = \begin{bmatrix} \frac{A_lE_l}{m_0}\sin^2\theta_0 + \frac{12E_lI_l}{m_0^3}\cos^2\theta_0 & -\left(\frac{A_lE_l}{m_0} - \frac{12E_lI_l}{m_0^3}\right)\sin\theta_0\cos\theta_0 & \frac{6E_lI_l}{m_0^2}\cos\theta_0 & -\frac{A_lE_l}{m_0}\sin^2\theta_0 - \frac{12E_lI_l}{m_0^3}\cos^2\theta_0 & \left(\frac{A_lE_l}{m_0} - \frac{12E_lI_l}{m_0^3}\right)\sin\theta_0\cos\theta_0 & \frac{6E_lI_l}{m_0^2}\cos\theta_0 \\ -\left(\frac{A_lE_l}{m_0} - \frac{12E_lI_l}{m_0^3}\right)\sin\theta_0\cos\theta_0 & \frac{A_lE_l}{m_0}\cos^2\theta_0 + \frac{12E_lI_l}{m_0^3}\sin^2\theta_0 & \frac{6E_lI_l}{m_0^2}\sin\theta_0 & (\frac{A_lE_l}{m_0} - \frac{12E_lI_l}{m_0^3})\sin\theta_0\cos\theta_0 & -\frac{A_lE_l}{m_0}\cos^2\theta_0 - \frac{12E_lI_l}{m_0^3}\sin^2\theta_0 & \frac{6E_lI_l}{m_0^2}\sin\theta_0 \\ \frac{6E_lI_l}{m_0^2}\cos\theta_0 & \frac{6E_lI_l}{m_0^2}\sin\theta_0 & \frac{4E_lI_l}{m_0} \quad \sqrt{a^2+b^2} & -\frac{6E_lI_l}{m_0^2}\cos\theta_0 & -\frac{6E_lI_l}{m_0^2}\sin\theta_0 & \frac{2E_lI_l}{m_0} \\ -\frac{A_lE_l}{m_0}\sin^2\theta_0 - \frac{12E_lI_l}{m_0^3}\cos^2\theta_0 & -\left(\frac{12E_lI_l}{m_0^3} - \frac{A_lE_l}{m_0}\right)\sin\theta_0\cos\theta_0 & -\frac{6E_lI_l}{m_0^2}\cos\theta_0 & \frac{A_lE_l}{m_0}\sin^2\theta_0 + \frac{12E_lI_l}{m_0^3}\cos^2\theta_0 & -\left(\frac{A_lE_l}{m_0} - \frac{12E_lI_l}{m_0^3}\right)\sin\theta_0\cos\theta_0 & -\frac{6E_lI_l}{m_0^2}\cos\theta_0 \\ -\left(\frac{12E_lI_l}{m_0^3} - \frac{A_lE_l}{m_0}\right)\sin\theta_0\cos\theta_0 & -\frac{A_lE_l}{m_0}\cos^2\theta_0 - \frac{12E_lI_l}{m_0^3}\sin^2\theta_0 & \frac{-6E_lI_l}{m_0^2}\sin\theta_0 & -\left(\frac{A_lE_l}{m_0l} - \frac{12E_lI_l}{m_0^3}\right)\sin\theta_0\cos\theta_0 & \frac{A_lE_l}{m_0}\cos^2\theta_0 + \frac{12E_lI_l}{m_0^3}\sin^2\theta_0 & -\frac{6E_lI_l}{m_0^2}\sin\theta_0 \\ \frac{6E_lI_l}{m_0^2}\cos\theta_0 & \frac{6E_lI_l}{m_0^2}\sin\theta_0 & \frac{2E_lI_l}{m_0} & -\frac{6E_lI_l}{m_0^2}\cos\theta_0 & \frac{-6E_lI_l}{m_0^2}\sin\theta_0 & \frac{4E_lI_l}{m_0} \end{bmatrix} \tag{A3}$$

Assembling of the global stiffness matrix as:

$$[K] = \begin{bmatrix} K_{11} & K_{12} & K_{13} & K_{14} & K_{15} & K_{16} & K_{17} & K_{18} & K_{19} \\ K_{21} & K_{22} & K_{23} & K_{24} & K_{25} & K_{26} & K_{27} & K_{28} & K_{29} \\ K_{31} & K_{32} & K_{33} & K_{34} & K_{35} & K_{36} & K_{37} & K_{38} & K_{39} \\ K_{41} & K_{42} & K_{43} & K_{44} & K_{45} & K_{46} & K_{47} & K_{48} & K_{49} \\ K_{51} & K_{52} & K_{53} & K_{54} & K_{55} & K_{56} & K_{57} & K_{58} & K_{59} \\ K_{61} & K_{62} & K_{63} & K_{64} & K_{65} & K_{66} & K_{67} & K_{68} & K_{69} \\ K_{71} & K_{72} & K_{73} & K_{74} & K_{75} & K_{76} & K_{77} & K_{78} & K_{79} \\ K_{81} & K_{82} & K_{83} & K_{84} & K_{85} & K_{86} & K_{87} & K_{88} & K_{89} \\ K_{91} & K_{92} & K_{93} & K_{94} & K_{95} & K_{96} & K_{97} & K_{98} & K_{99} \end{bmatrix}, \tag{A4}$$

Global thermal load is given as:

$$\{P\} = \begin{Bmatrix} E_hA_h\alpha_h\Delta T + E_lA_l\alpha_l\Delta T\sin\theta_0 \\ -E_lA_l\alpha_l\Delta T\cos\theta_0 \\ 0 \\ -E_hA_h\alpha_h\Delta T - E_lA_l\alpha_l\Delta T\sin\theta_0 \\ -E_lA_l\alpha_l\Delta T\cos\theta_0 \\ 0 \\ 0 \\ 2EA\alpha\Delta T\cos\theta_0 \\ 0 \end{Bmatrix} \tag{A5}$$

Applying boundary conditions leads to

$$\begin{bmatrix} K'_{11} & K'_{12} & K'_{13} \\ K'_{21} & K'_{22} & K'_{23} \\ K'_{31} & K'_{32} & K'_{33} \end{bmatrix} \begin{Bmatrix} u_1 \\ u_2 \\ u_3 \end{Bmatrix} = \begin{Bmatrix} P'_1 \\ P'_2 \\ P'_3 \end{Bmatrix}, \tag{A6}$$

where

$$K'_{11} = \frac{A_hE_h}{l_0} + \frac{A_lE_l}{m_0}\sin^2\theta_0 + \frac{12E_lI_l}{m_0^3}\cos^2\theta_0, \tag{A7}$$

$$K'_{12} = K'_{21} = -\frac{A_hE_h}{l_0}, \tag{A8}$$

$$K'_{13} = K'_{31} = -\frac{A_lE_l}{m_0}\sin^2\theta_0 - \frac{12E_lI_l}{m_0^3}\cos^2\theta_0 - \tan\varphi\left(\frac{12E_lI_l}{m_0^3} - \frac{A_lE_l}{m_0}\right)\sin\theta_0\cos\theta_0, \tag{A9}$$

$$K'_{22} = \frac{A_hE_h}{l_0} + \frac{A_lE_l}{m_0}\sin^2\theta_0 + \frac{12E_lI_l}{m_0^3}\cos^2\theta_0, \tag{A10}$$

$$K'_{23} = K'_{32} = -\frac{A_lE_l}{m_0}\sin^2\theta_0 - \frac{12E_lI_l}{m_0^3}\cos^2\theta_0 + \tan\varphi\left(\frac{12E_lI_l}{m_0^3} - \frac{A_lE_l}{m_0}\right)\sin\theta_0\cos\theta_0, \tag{A11}$$

$$K'_{33} = 2\left(\frac{A_lE_l}{m_0}\sin^2\theta_0 + \frac{12E_lI_l}{m_0^3}\cos^2\theta_0\right) + 2\tan^2\varphi\left(\frac{A_lE_l}{m_0}\cos^2\theta_0 + \frac{12E_lI_l}{m_0^3}\sin^2\theta_0\right), \tag{A12}$$

$$\{P'\} = \begin{Bmatrix} E_hA_h\alpha_h\Delta T + E_lA_l\alpha_l\Delta T\sin\theta_0 \\ -E_hA_h\alpha_h\Delta T - E_lA_l\alpha_l\Delta T\sin\theta_0 \\ 2E_lA_l\alpha_l\Delta T\cos\theta_0\tan\varphi \end{Bmatrix}. \tag{A13}$$

Appendix B

The mechanical properties of the proposed metamaterials are investigated under tension using FEA. In the simulations, a 4 × 4 unit cell assembled metamaterial is considered (see Fig. 9 (a)). A uniaxial displacement (10 mm) loading is applied on the top plate within the elastic limit, while the bottom plate is fixed along both the x and y directions. Three proposed metamaterial designs #A, #B, and #D are selected ($A_h/A_l = 2.5$). Several material combinations including Al/Ti, Iron-Invar, Al6061/Ti-6Al-4V, PEGDA/Cu-PEGDA, Teflon/Acrylic and customized materials A/B are considered. The material properties of these constitutive materials are shown in Table 1. The FEA results are shown in Table 2.

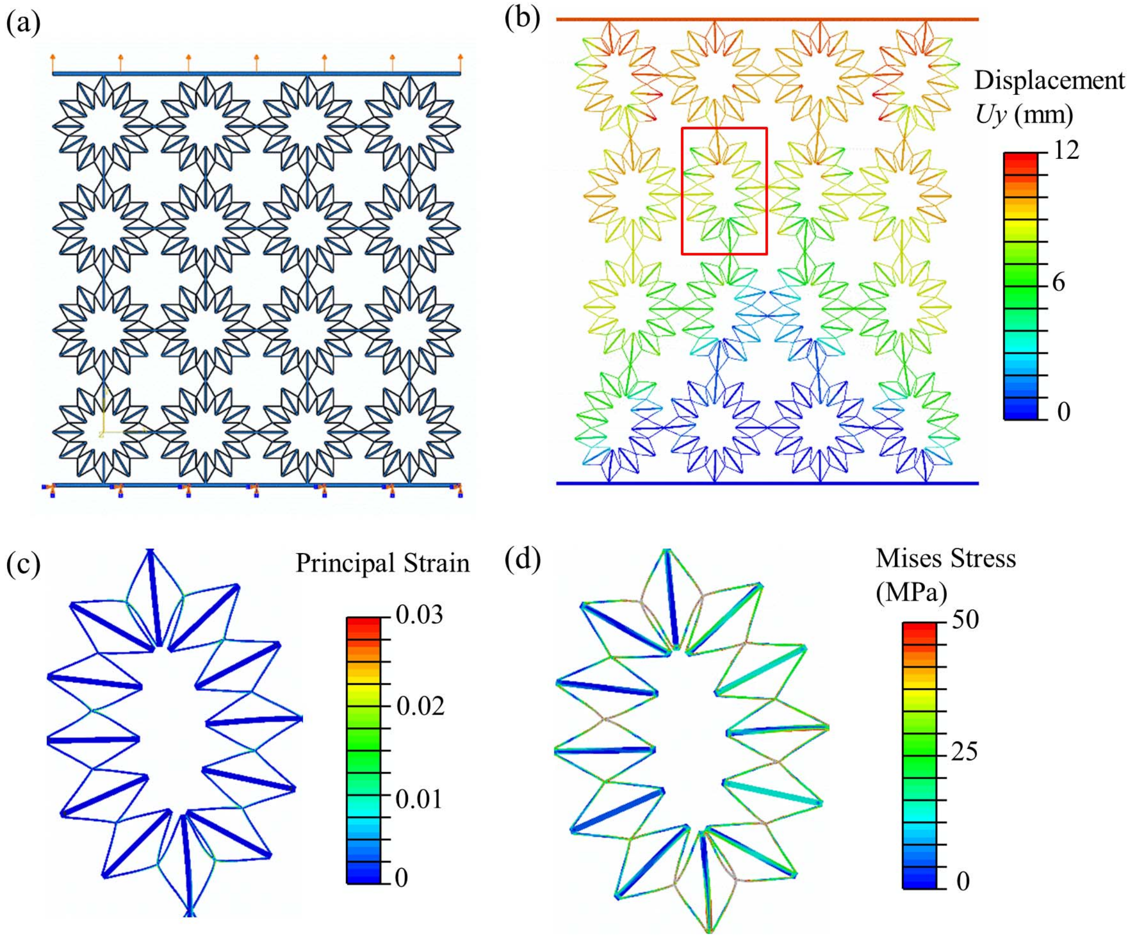

Fig. 9. Finite element model of the bi-material metamaterial #D ($R_0 = 10$ mm, $\theta_0 = 60°$, $n = 24$) under tension. (a) Undeformed configuration. (b) Deformed configuration. (c) FEA results of the maximum principal strain. (c) FEA results of the Mises stress.

References

[1] Zhang Y, Zhang F, Yan Z, Ma Q, Li X, Huang Y, et al. Printing, folding and assembly methods for forming 3D mesostructures in advanced materials. Nat Rev Mater 2017;2:17019.

[2] Wang Q, Jackson JA, Ge Q, Hopkins JB, Spadaccini CM, Fang NX. Lightweight mechanical metamaterials with tunable negative thermal expansion. Phys Rev Lett 2016;117:175901.

[3] Chen Y, Li T, Scarpa F, Wang L. Lattice metamaterials with mechanically tunable Poisson's ratio for vibration control. Phys Rev Appl 2017;7:024012.

[4] Babaee S, Shim J, Weaver JC, Chen ER, Patel N, Bertoldi K. 3D Soft metamaterials with negative Poisson's ratio. Adv Mater 2013;25:5044–9.

[5] Li T, Hu X, Chen Y, Wang L. Harnessing out-of-plane deformation to design 3D architected lattice metamaterials with tunable Poisson's ratio. Sci Rep 2017;7:8949.

[6] Li T, Wang L. Bending behavior of sandwich composite structures with tunable 3D-printed core materials. Compos Struct 2017;175:46–57.

[7] Vogiatzis P, Chen S, Wang X, Li T, Wang L. Topology optimization of multi-material negative Poisson's ratio metamaterials using a reconciled level set method. Comput Aided Des 2017;83:15–32.

[8] Zheng X, Lee H, Weisgraber TH, Shusteff M, DeOtte J, Duoss EB, et al. Ultralight, ultrastiff mechanical metamaterials. Science 2014;344:1373–7.

[9] Chen Y, Li T, Jia Z, Scarpa F, Yao C-W, Wang L. 3D printed hierarchical honeycombs with shape integrity under large compressive deformations. Mater Des 2018;137:226–34.

[10] Hewage TA, Alderson KL, Alderson A, Scarpa F. Double-negative mechanical metamaterials displaying simultaneous negative stiffness and negative Poisson's ratio properties. Adv Mater 2016;28:10323–32.

[11] Chen Y, Jia Z, Wang L. Hierarchical honeycomb lattice metamaterials with improved thermal resistance and mechanical properties. Compos Struct 2016;152:395–402.

[12] Chen Y, Wang L. Harnessing structural hierarchy to design stiff and lightweight phononic crystals. Extreme Mech Lett 2016;9:91–6.

[13] Gansel JK, Thiel M, Rill MS, Decker M, Bade K, Saile V, et al. Gold helix photonic metamaterial as broadband circular polarizer. Science 2009;325:1513–5.

[14] Lightfoot P, Woodcock DA, Maple MJ, Villaescusa LA, Wright PA. The widespread occurrence of negative thermal expansion in zeolites. J Mater Chem 2001;11:212–6. [Basis of a presentation given at Materials Discussion No. 3, 26-29 September, 2000, University of Cambridge, UK].

[15] Sheng J, Wang L, Li D, Cao W, Feng Y, Wang M, et al. Thermal expansion behavior of copper matrix composite containing negative thermal expansion PbTiO3 particles. Mater Des 2017;132:442–7.

[16] Kofteros M, Rodriguez S, Tandon V, Murr L. A preliminary study of thermal expansion compensation in cement by ZrW_2O_8 additions. Scr Mater 2001;45:369–74.

[17] Yang Q, Zhang P, Cheng L, Min Z, Chyu M, To AC. Finite element modeling and validation of thermomechanical behavior of Ti-6Al-4V in directed energy deposition additive manufacturing. Addit Manuf 2016;12:169–77.

[18] Yangbo L, Dahai H, Jianshu O. Fast algorithms of the simulation analysis of the thermal stresses on concrete dams during construction periods. Physics Procedia 2012;24:1171–7.

[19] Mukherjee T, Zhang W, DebRoy T. An improved prediction of residual stresses and distortion in additive manufacturing. Comput Mater Sci 2017;126:360–72.

[20] Berger J, Mercer C, McMeeking RM, Evans AG. The design of bonded bimaterial lattices that combine low thermal expansion with high stiffness. J Am Ceram Soc 2011;94:s42–54.

[21] Gdoutos E, Shapiro AA, Daraio C. Thin and thermally stable periodic metastructures. Exp Mech 2013;53:1735–42.

[22] Hopkins JB, Song Y, Lee H, Fang NX, Spadaccini CM. Polytope sector-based synthesis and analysis of microstructural architectures with tunable thermal conductivity and expansion. J Mech Des 2016;138:10.

[23] Miller W, Mackenzie DS, Smith CW, Evans KE. A generalised scale-independent mechanism for tailoring of thermal expansivity: positive and negative. Mech Mater 2008;40:351–61.

[24] Palumbo NMA, Smith CW, Miller W, Evans KE. Near-zero thermal expansivity 2-D lattice structures: performance in terms of mass and mechanical properties. Acta Mater 2011;59:2392–403.

[25] Steeves CA, Mercer C, Antinucci E, He MY, Evans AG. Experimental investigation of the thermal properties of tailored expansion lattices. Int J Mech Mater Des 2009;5:195–202.

[26] Wei K, Chen H, Pei Y, Fang D. Planar lattices with tailorable coefficient of thermal expansion and high stiffness based on dual-material triangle unit. J Mech Phys Solids 2016;86:173–91.

[27] Xu H, Pasini D. Structurally efficient three-dimensional metamaterials with controllable thermal expansion. Sci Rep 2016;6:34924.

[28] Ai L, Gao XL. Metamaterials with negative Poisson's ratio and non-positive thermal expansion. Compos Struct 2017;162:70–84.

[29] Takenaka K. Negative thermal expansion materials: technological key for control of thermal expansion. Sci Technol Adv Mater 2012;13:013001.

[30] Sigmund O, Torquato S. Composites with extremal thermal expansion coefficients. Appl Phys Lett 1996;69:3203–5.

[31] Ng CK, Saxena KK, Das R, Saavedra Flores EI. On the anisotropic and negative thermal expansion from dual-material re-entrant-type cellular metamaterials. J Mater Sci 2016;52:899–912.

[32] Zammit V, Gatt R, Farrugia PS, Grima JN. A system with adjustable positive or negative thermal expansion. Proc R Soc A Math Phys Eng Sci 2007;463:1585–96.

[33] Jefferson G, Parthasarathy TA, Kerans RJ. Tailorable thermal expansion hybrid structures. Int J Solids Struct 2009;46:2372–87.

[34] Steeves CA, dos Santos e Lucato SL, He M, Antinucci E, Hutchinson JW, Evans AG. Concepts for structurally robust materials that combine low thermal expansion with high stiffness. J Mech Phys Solids 2007;55:1803–22.

[35] Takezawa A, Kobashi M, Kitamura M. Porous composite with negative thermal expansion obtained by photopolymer additive manufacturing. APL Mater 2015;3:076103.

[36] Qi J, Halloran JW. Negative thermal expansion artificial material from iron-nickel alloys by oxide co-extrusion with reductive sintering. J Mater Sci 2004;39:6.

[37] Ha CS, Hestekin E, Li J, Plesha ME, Lakes RS. Controllable thermal expansion of large magnitude in chiral negative Poisson's ratio lattices. Phys Status Solidi (b) 2015;252:1431–4.

[38] Wu L, Li B, Zhou J. Isotropic negative thermal expansion metamaterials. ACS Appl Mater Interfaces 2016;8:17721–7.

[39] Yeung HH, Kilmurray R, Hobday CL, McKellar SC, Cheetham AK, Allan DR, et al. Hidden negative linear compressibility in lithium l-tartrate. PCCP 2017;19:3544–9.

[40] Dudek KK, Attard D, Caruana-Gauci R, Wojciechowski KW, Grima JN. Unimode metamaterials exhibiting negative linear compressibility and negative thermal expansion. Smart Mater Struct 2016;25:025009.

[41] Mousanezhad D, Haghpanah B, Ghosh R, Hamouda AM, Nayeb-Hashemi H, Vaziri A. Elastic properties of chiral, anti-chiral, and hierarchical honeycombs: a simple energy-based approach. Theor Appl Mech Lett 2016;6:81–96.

[42] Boatti E, Vasios N, Bertoldi K. Origami metamaterials for tunable thermal expansion. Adv Mater 2017;29:1700360.

[43] Liu J, Gu T, Shan S, Kang SH, Weaver JC, Bertoldi K. Harnessing buckling to design architected materials that exhibit effective negative swelling. Adv Mater 2016;28:6619–24.

[44] Lehman J, Lakes R. Stiff lattices with zero thermal expansion. J Intell Mater Syst Struct 2012;23:1263–8.

[45] Qu J, Kadic M, Naber A, Wegener M. Micro-structured two-component 3D metamaterials with negative thermal-expansion coefficient from positive constituents. Sci Rep 2017;7:40643.

[46] Yamamoto N, Gdoutos E, Toda R, White V, Manohara H, Daraio C. Thin films with ultra-low thermal expansion. Adv Mater 2014;26:3076–80.

[47] Pryde AKA, Hammonds KD, Dove MT, Heine V, Gale JD, Warren MC. Origin of the negative thermal expansion in ZrW2O8 and ZrV2O7. J Phys: Condens Matter 1996;8:10.

[48] Takenaka K, Okamoto Y, Shinoda T, Katayama N, Sakai Y. Colossal negative thermal expansion in reduced layered ruthenate. Nat Commun 2017;8:14102.

[49] Sapnik AF, Liu X, Boström HLB, Coates CS, Overy AR, Reynolds EM, et al. Negative thermal expansion and metallophilicity in $Cu_3[Co(CN)_6]$, 2017, arXiv:1702.07133.

[50] Hoberman C. Reversibly expandable doubly-curved truss structure. Google Patents 1990.

[51] Xu H, Farag A, Pasini D. Multilevel hierarchy in bi-material lattices with high specific stiffness and unbounded thermal expansion. Acta Mater 2017;134:155–66.